Mingyuan Ge[1]
National Synchrotron Light Source II (NSLS-II),
Brookhaven National Laboratory,
Upton, NY 11973
e-mail: mingyuan@bnl.gov

Wenjun Liu
Advanced Photon Source (APS),
Argonne National Laboratory,
Argonne, IL 60439
e-mail: wjliu@anl.gov

David C. Bock
Institute for Electrochemically Stored Energy,
Stony Brook University,
Stony Brook, NY 11974;
Interdisciplinary Science Department,
Brookhaven National Laboratory,
Upton, NY 11973
e-mail: david.bock@stonybrook.edu

Vincent De Andrade
Advanced Photon Source (APS),
Argonne National Laboratory,
Argonne, IL 60439
e-mail: vdeandrade@anl.gov

Hanfei Yan
National Synchrotron Light Source II (NSLS-II),
Brookhaven National Laboratory,
Upton, NY 11973
e-mail: hyan@bnl.gov

Xiaojing Huang
National Synchrotron Light Source II (NSLS-II),
Brookhaven National Laboratory,
Upton, NY 11973
e-mail: xjhuang@bnl.gov

Kenneth J. Takeuchi
Department of Chemistry;
Department of Materials Science and
Chemical Engineering;
Institute for Electrochemically Stored Energy,
Stony Brook University,
Stony Brook, NY 11974;
Interdisciplinary Science Department,
Brookhaven National Laboratory,
Upton, NY 11973
e-mail: kenneth.takeuchi.1@stonybrook.edu

Amy C. Marschilok
Department of Chemistry;
Department of Materials Science and
Chemical Engineering;
Institute for Electrochemically Stored Energy,
Stony Brook University,
Stony Brook, NY 11974;
Interdisciplinary Science Department,
Brookhaven National Laboratory,
Upton, NY 11973
e-mail: amy.marschilok@stonybrook.edu

X-Ray Induced Chemical Reaction Revealed by In Situ X-Ray Diffraction and Scanning X-Ray Microscopy in 15 nm Resolution

The detection sensitivity of synchrotron-based X-ray techniques has been largely improved due to the ever-increasing source brightness, which has significantly advanced ex situ and in situ research for energy materials such as lithium-ion batteries. However, the strong beam–material interaction arising from the high beam flux can substantially modify the material structure. The beam-induced parasitic effect inevitably interferes with the intrinsic material property, making the interpretation of the experimental results difficult and requiring comprehensive assessments. Here, we present a quantitative study of the beam effect on an electrode material $Ag_2VO_2PO_4$ using four different X-ray characterization methods with different radiation dose rates. The material system exhibits interesting and reversible radiation-induced thermal and chemical reactions, further evaluated under electron microscopy to illustrate the underlying mechanism. The work will provide a guideline for using synchrotron X-rays to distinguish the intrinsic behavior from extrinsic structure change of materials induced by X-rays. [DOI: 10.1115/1.4054952]

Keyword: advanced materials characterization

[1]Corresponding authors.
Manuscript received March 1, 2022; final manuscript received May 19, 2022; published online July 18, 2022. Assoc. Editor: Johanna Nelson Weker.

Esther S. Takeuchi
Department of Chemistry;
Department of Materials Science and Chemical Engineering;
Institute for Electrochemically Stored Energy,
Stony Brook University,
Stony Brook, NY 11974;
Interdisciplinary Science Department,
Brookhaven National Laboratory,
Upton, NY 11973
e-mail: Esther.Takeuchi@stonybrook.edu

Huolin Xin
Center for Functional Nanomaterials (CFN),
Brookhaven National Laboratory,
Upton, NY 11973;
Department of Physics and Astronomy,
University of California,
Irvine, CA 92697
e-mail: huolin.xin@uci.edu

Yong S. Chu[1]
National Synchrotron Light Source II (NSLS-II),
Brookhaven National Laboratory,
Upton, NY 11973
e-mail: ychu@bnl.gov

1 Introduction

As a cost-efficient and environment-friendly energy storage device, the lithium-ion battery has been widely used in portable electronics and has envisaged rapid exploration in recent decades. One of the biggest challenges in the battery research field is gaining a mechanistic understanding of the electrode material under working conditions, which plays a pivotal role in designing new materials to advance battery performance. Apart from the ensemble-averaged electrochemical measurements, in situ characterization at the nanoscale can provide profound information to understand the underlying physics, which is possible using the state-of-the-art imaging techniques using synchrotron X-rays or electrons. For instance, X-ray diffraction (XRD) and X-ray absorption spectroscopy are highly sensitive to crystal structure and chemical states. Both have been widely used to study the phase transition [1–3] and lattice distortion [4–7] of battery materials during the charging/discharging process [8–10]. Different from X-ray spectroscopic techniques, X-ray microscopy provides direct imaging capability. It is superior in visualizing the material morphology and element distribution in three dimensions and has gained significance in the battery study to uncover the morphology-dependent electrode behavior [11–15]. Complementary to X-rays, advanced electron microscopy can provide atomic imaging and analysis with sub-angstrom resolution and therefore is making encouraging progress in the ex situ and in situ study in the battery research [16]. Combining X-rays and electron microscopy makes multi-modality characterization from the atomic scale to micron size technically feasible.

The increasing brightness of the X-ray sources vastly improves the detection sensitivity. However, strong beam–material interaction will inevitably induce parasitic effects to modify the material structure, including beam-induced water radiolysis [17,18], point-defect generation at crystal interfaces [19], soft-(bio-)material destruction [20–23], and complicated phase transition that involves a subtle change of electronic states inside the material [24]. More recently, battery materials have been reported to suffer significant structure change under X-rays and electron beams, and the beam effect is very material-specific and sensitive to dosage [25–27]. Here, we will take one specific battery material ($Ag_2VO_2PO_4$) as an example to illustrate the thermal and non-thermal effects of X-ray and electron beams, which are intensely dependent on the total beam dose and dose rate.

$Ag_2VO_2PO_4$ has layered structure with space group of C12/m1 (lattice: $a = 12.43$, $b = 6.298$, $c = 6.3$ (unit Angstrom), $\alpha = 90$ deg, $\beta = 90.38$ deg, $\gamma = 90$ deg) [28]. P–O and V–O form the tetrahedral and octahedral framework inside the crystal, with Ag atoms sitting inside the layer channel. It is widely used as a cathode material in primary batteries. Despite being electronically resistive, $Ag_2VO_2PO_4$ undergoes a fold of 15,000 decreases in impedance upon initial discharge, making the material an excellent candidate for powering biomedical devices such as pacemakers that require high pulse power [28,29]. There is a strong scientific interest to monitor the structure evolution that contributes to the impedance decrease using microscopy characterization techniques such as X-rays and electrons. Consequently, it is essential to evaluate the beam–material interaction accurately as the first step to distinguish the intrinsic material response from the extrinsic effect induced by external fields of either X-ray or electron beams.

2 Results and Discussion

Four X-ray techniques are employed to study the beam effects on $Ag_2VO_2PO_4$, which involve synchrotron-based white beam X-ray Laue diffraction, monochromatic XRD, hard X-ray nanoprobe (HXN), and transmission X-ray microscopy (TXM). The photon flux is estimated at 10^{13}–10^{14}, 10^9, 10^8, and 10^{11} photon s^{-1}, respectively. We report that the material system exhibits interesting and reversible radiation-induced thermal and chemical reactions, as revealed by the XRD and the high resolution (15 nm) imaging using HXN [29,30]. Meanwhile, the interaction of the material with electron beam irradiation was also studied using transmission electron microscopy (TEM) to illustrate the underlying mechanism. In the following, we present the structure change of $Ag_2VO_2PO_4$ under X-ray irradiation with high dose (white/monochromatic X-ray) and median-to-low dose (HXN and TXM) to distinguish between the dose-dependent thermal effect and photon-induced chemical reaction.

2.1 White/Monochromatic X-Ray Diffraction. In the first experiment, we study the beam effect with white/monochromatic

XRD at high X-ray doses. A white beam in an energy range of 7–40 keV was used to produce Laue diffraction patterns for providing an overview of the crystalline structure. The exposure time was either 1 s or 5 min. Energy-adjustable monochromatic X-ray beam was used to perform energy scans through individual diffraction spots to characterize the crystalline lattice deformation. The exposure time for a monochromatic beam scan was 16 min. In the experiment, we alternately used the white and monochromatic beams to deliver high-level X-ray dose (with the white beam) and monitor the beam effect by scanning the diffraction spots (with the monochromatic beam). Details of the experiment can be found in Section 4.

Figure 1(*a*) shows the Laue diffraction pattern of a pristine $Ag_2VO_2PO_4$ single crystal. The surface-normal direction parallel to the beam illumination was [1 0 0]. Figure 1(*b*) shows the diffraction pattern for the same specimen after irradiation with white/mono X-rays (see Section 4 for details). After illumination, the intensities of most diffraction spots are weakened without developing additional diffraction spots, indicating that the crystalline structure was deteriorating without undergoing a phase transformation. Figure 1(*c*) depicts the integrated intensity of (1–10) diffraction in the reciprocal space obtained from the monochromatic beam scan. The solid lines refer to the results of successive monochromatic beam scans, and dashed lines correspond to the results after the 5-min white beam exposure. We note that the peak position of (1–10) remains constant under the mono-beam scan, with slight variations between different scans ($33.732 \pm 0.005\ nm^{-1}$).

In comparison, a significant variation of peak position is found after white beam exposure ($33.729 \pm 0.020\ nm^{-1}$), e.g., scan #5, #6, and #11. In Fig. 1(*d*), we plot the evolution of peak intensity and peak width derived from Fig. 1(*c*). The noticeable decrease of the peak intensity and increase in peak width suggest that the material gradually loses its crystalline structure (or crystalline volume) after white beam illumination.

We use finite element analysis (FEA) to estimate the thermal effect induced by X-rays. In line with the experiment configuration, under white beam illumination, the energy transferred to the material is 1–3 mW with a beam flux of 10^{13} photons s^{-1}. FEA shows that the temperature in the center of the beam will increase to ~500 °C, close to the melting point of the $Ag_2VO_2PO_4$ crystal (526 °C; see Supplemental Materials on the ASME Digital Collection). In contrast, the monochromatic beam only transfers sub-μW

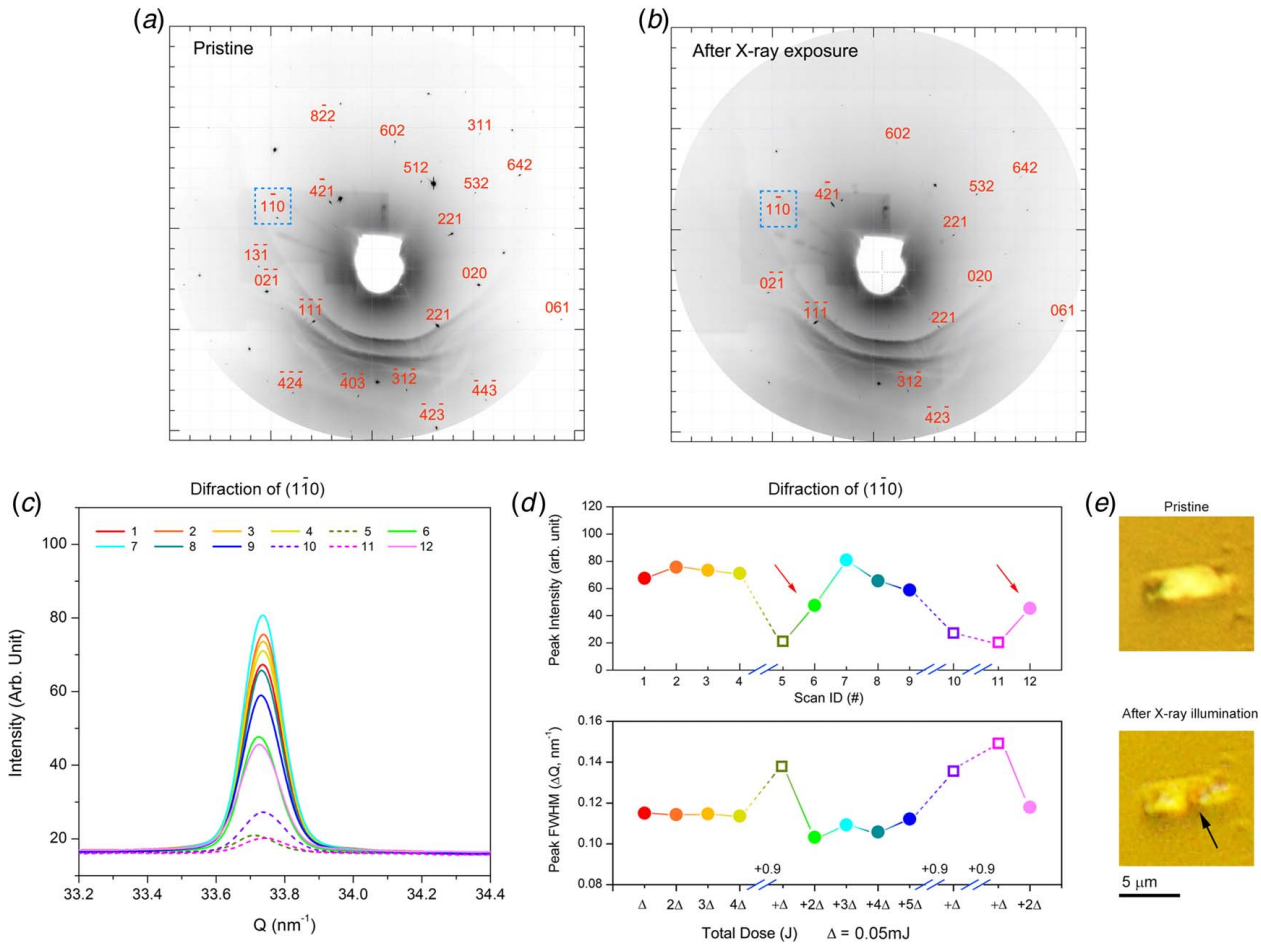

Fig. 1 In situ white/mono-beam XRD shows an evolution of (1 −1 0) diffraction intensity profile due to alternating exposure to the monochromatic and white X-ray beam. (*a*) White beam diffraction pattern obtained from a pristine sample. (*b*) White beam diffraction pattern from a sample with considerable exposure to white and monochromatic beam. (*c*) Successive measurement of the (1 −1 0) diffraction profile was taken by scanning the energy of the monochromatic beam from 13 to 20 keV. The diffraction profiles in solid lines were obtained by successive energy scans. The diffraction profiles in dashed lines were obtained by performing an energy scan after exposing the sample to a white beam for 5 min. Due to each white beam exposure, the energy transferred to the sample is estimated to be 3×10^{-3} W (dose: ~0.9 J) over the sample. The estimated energy transfer due to each monochromatic X-ray energy scan is 5×10^{-8} W (dose: ~5×10^{-5} J). (*d*) The integrated intensity and the full width at half maximum of the (1 −1 0) diffraction profiles are as shown in (*c*). The red arrows indicate a recovery of peak intensity and reduction of peak width right after switching from the white beam to the monochromatic beam. (*e*) Optical images show the morphology of the sample before and after the beam illumination. The arrow indicates the beam position.

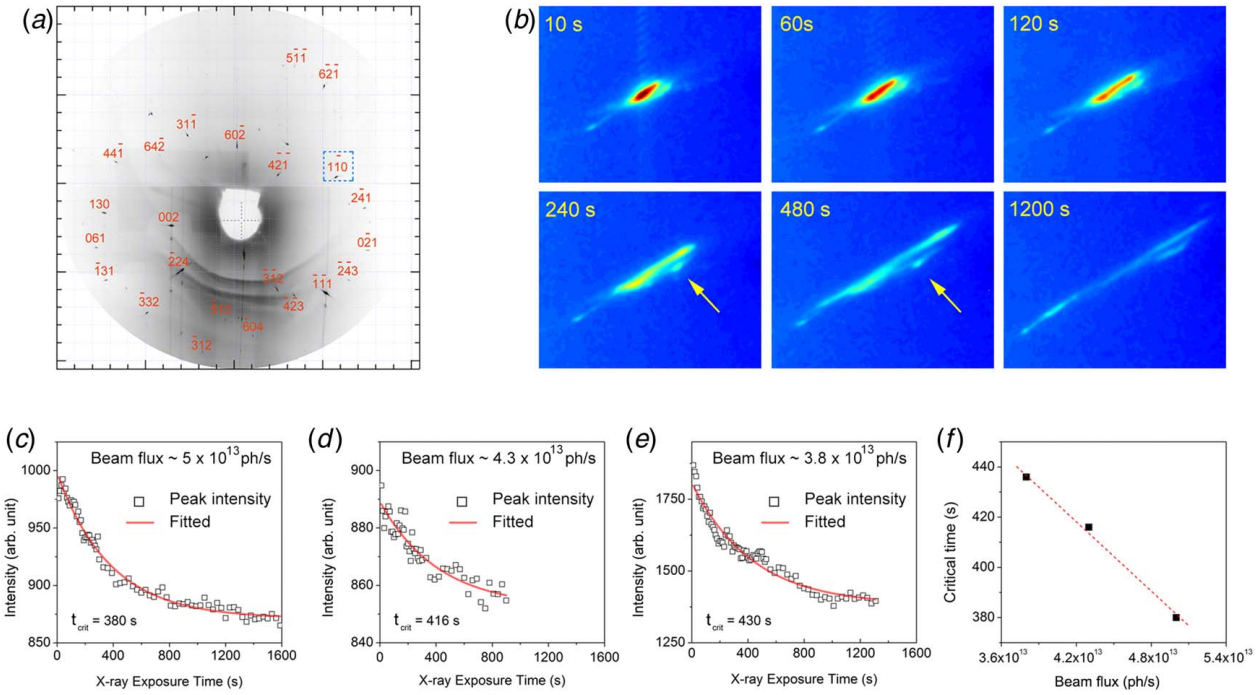

Fig. 2 Crystal structure modification under white beam X-ray exposure. (*a*) A white beam diffraction pattern of another new $Ag_2VO_2PO_4$ single crystal. (*b*) 2D images illustrate the real-time evolution of (1 −1 0) diffraction under white beam illumination with a flux of $\sim 5 \times 10^{13}$ photons s^{-1}. The arrows indicate the additional diffraction spots formation. (*c*) Integrated diffraction intensity from (*b*) shows exponential decay. (*d*) and (e) Integrated diffraction intensity under two other conditions with beam flux of $\sim 4.3 \times 10^{13}$ photons s^{-1} and $\sim 3.8 \times 10^{13}$ photons s^{-1}, respectively. (*f*) The critical time derived from the curve fitting of $I = I_0 \exp(t/t_{crit})$ is inversely proportional to the beam flux.

to the crystal, and the temperature increase in the sample is negligible. It is feasible that the material experiences re-crystallization when the white beam is switched off. As shown in Fig. 1(*d*), we found an instant recovery of peak intensity and narrower peak width right after switching from white beam to monochromatic beam (scans #6 and #12 in Fig. 1(*b*)). We can also observe the material structure/morphology change from the optical images, as shown in Fig. 1(*e*).

To gain additional insights into the crystal structure change, we recorded a series of 2D snapshots of (1–10) diffraction from a fresh crystal. Figure 2(*a*) shows the Laue diffraction. Figure 2(*b*) shows the real-time measurements of the (1–10) diffraction under

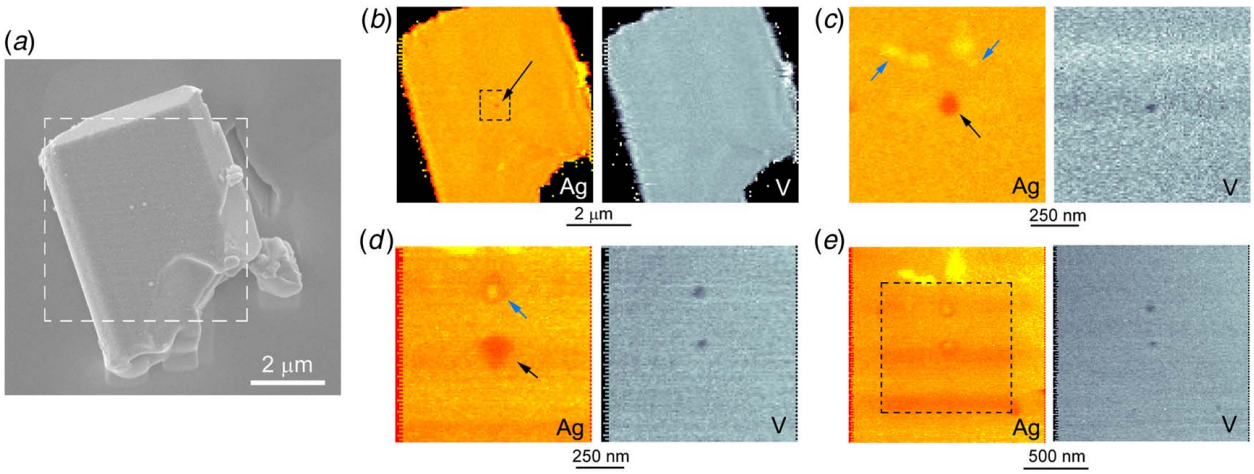

Fig. 3 Ag reduction and redistribution under a monochromatic nano-beam of 15 nm × 15 nm in size. Energy transferred to the material is estimated to be 10^{-8} W and 10^{-11} W nm^{-2} for HXN. (*a*) SEM image of a $AgVO_2PO_4$ crystal. (*b*) XRF images of Ag and V of the same crystal as shown in (*a*), produced by a 2D fly-scan with 0.1 dwell time per pixel. (*c*) XRF images of Ag and V after resting the beam for 3 min. (*d*) XRF images of Ag and V after resting the beam at a new position for 10 min. (*e*) Scan with a large field of view shows a stripe pattern in the Ag image, indicating the Ag redistribution. The dashed box indicates the region in the last scan shown in (*d*). Note: in (*b*)–(*d*), the black arrow indicates Ag deficiency. Blue arrows indicate additional Ag spots formation. Note: for the XRF image of Ag showing in (*b*)–(*e*), the darker spot/shadow in a more reddish color indicates lower Ag concentration. Similarly, for the XRF image of V showing in (*b*)–(*e*), the darker spot/shadow indicates lower V concentration.

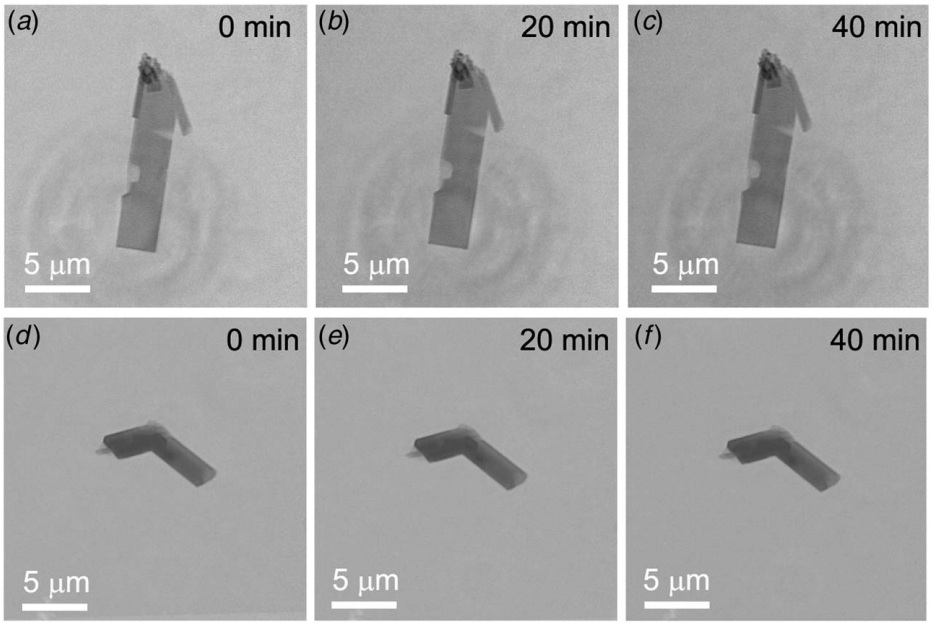

Fig. 4 TXM image of two crystals at different exposure times. Images were taken at 8 keV. (*a*)–(c) Morphology of particle #1 after 0 min, 20 min, and 40 min exposure. (*d*)–(*f*) Morphology of particle #2 after 0 min, 20 min, and 40 min exposure.

Table 1 Comparison of X-ray techniques

Experiment	Beam energy (keV)	Beam size ($\mu m \times \mu m$)	Average flux (ph s^{-1})	Flux per area (s^{-1} nm^{-2})	Beam energy (W)	Energy transfer to material (W)	Energy transfer to material per area (W nm^{-2})
White beam diffraction	7–30	0.5×0.5	$\sim 6 \times 10^{13}$	$\sim 2.4 \times 10^{8}$	$\sim 3 \times 10^{-2}$	$\sim 3 \times 10^{-3}$	$\sim 1.2 \times 10^{-8}$
Mono-beam diffraction	18	0.5×0.5	$\sim 1 \times 10^{9}$	$\sim 4 \times 10^{3}$	$\sim 2.6 \times 10^{-6}$	$\sim 5.3 \times 10^{-8}$	$\sim 2 \times 10^{-13}$
HXN	12	0.015×0.015	$\sim 2 \times 10^{8}$	$\sim 9 \times 10^{5}$	$\sim 3.8 \times 10^{-7}$	$\sim 1.2 \times 10^{-8}$	$\sim 5 \times 10^{-11}$
TXM	8	60×60	$\sim 1.5 \times 10^{11}$	$\sim 4 \times 10^{1}$	$\sim 2 \times 10^{-4}$	$\sim 1 \times 10^{-7}$	$\sim 3 \times 10^{-15}$

Note: Sample size is about 30 $\mu m^2 \times 1$ μm.

the white beam with a flux of $\sim 5.0 \times 10^{13}$ photons s^{-1}. During the first 60 s of exposure, a well-defined diffraction spot gradually broadened. After 120 s, the diffraction peak splits into two lobes and elongates in the transverse direction, indicating the generation of another crystalline domain with a different orientation. After 240 s of exposure, another separate diffraction spot emerges, suggesting the creation of a third small crystal with a different orientation. Further broadening of the diffraction spot up to 1200 s indicates substantial deterioration and distortion of the crystalline lattice. A complete evolution snapshot can be found in the Supplemental Materials on the ASME Digital Collection.

In Fig. 2(*c*), the intensity, integrated over the diminishing diffraction spot, is plotted with the exposure time. The integrated intensity is described by an exponential decay with a formula of $I = I_0 \exp(t/t_{crit})$, where I is the integrated peak intensity, t is the X-ray exposure time, and t_{crit} is determined to be 380 s. The exponential decay of the diffraction intensity indicates continuous deterioration of crystalline volume fraction, which is consistent with the induced temperature increase that is close to the melting point of the crystal, as predicted by the FEA simulation. Peak intensity under two other different beam fluxes ($\sim 4.3 \times 10^{13}$ and 3.8×10^{13} photon s^{-1}) was also recorded (Figs. 2(*d*) and 2(*e*)), and t_{crit} is fitted to be 416 s and 430 s, respectively. We note that the derived t_{crit} is inversely proportional to the beam flux (Fig. 2(*f*)). We conclude that the thermal effect is dominant under the white beam.

In the next step, we evaluate the beam–material interaction under relative weak beams, such as a monochromatic beam with a beam flux that is 4–6 orders less than the white beam. For example, scrutinizing the peak intensity change in Fig. 1 discloses a slight intensity decrease under successive mono-beam acquisitions, such as scans #3, #4, #8, and #9. The observed intensity decrease infers that the crystal suffers from other types of beam–material interaction other than the thermal effect. It is well known that regular photographic paper will get exposed to light and trigger the decomposition of AgBr to form fine Ag particles [31]. In the following, we will demonstrate a similar Ag reduction in $Ag_2VO_2PO_4$ when subjected to X-ray illumination, which is responsible for the peak intensity decrease, as shown in Fig. 2.

2.2 Hard X-Ray Nanoprobe and Transmission X-Ray Microscopy Characterizations. The HXN at the National Synchrotron Light Source II (NSLS-II) produces an X-ray beam size of ~10 nm [29,32]. Here we use the HXN for investigating the beam-material effect in $Ag_2VO_2PO_4$. Figure 3(*a*) shows the scanning electron microscopy (SEM) image of the $Ag_2VO_2PO_4$ particle. The dashed square region in Fig. 3(*a*) indicates the sample area scanned at HXN to map out the Ag and vanadium (V) distributions, as the X-ray fluorescence (XRF) image shown in Fig. 3(*b*). The image contrast encodes the element concentration. Based on the first scan, Ag and V intensities were well-correlated and uniformly distributed throughout the sample. However, we discovered a small region with Ag deficiency at the center of the Ag mapping, which was absent in the pristine SEM image. Note that the X-ray beam

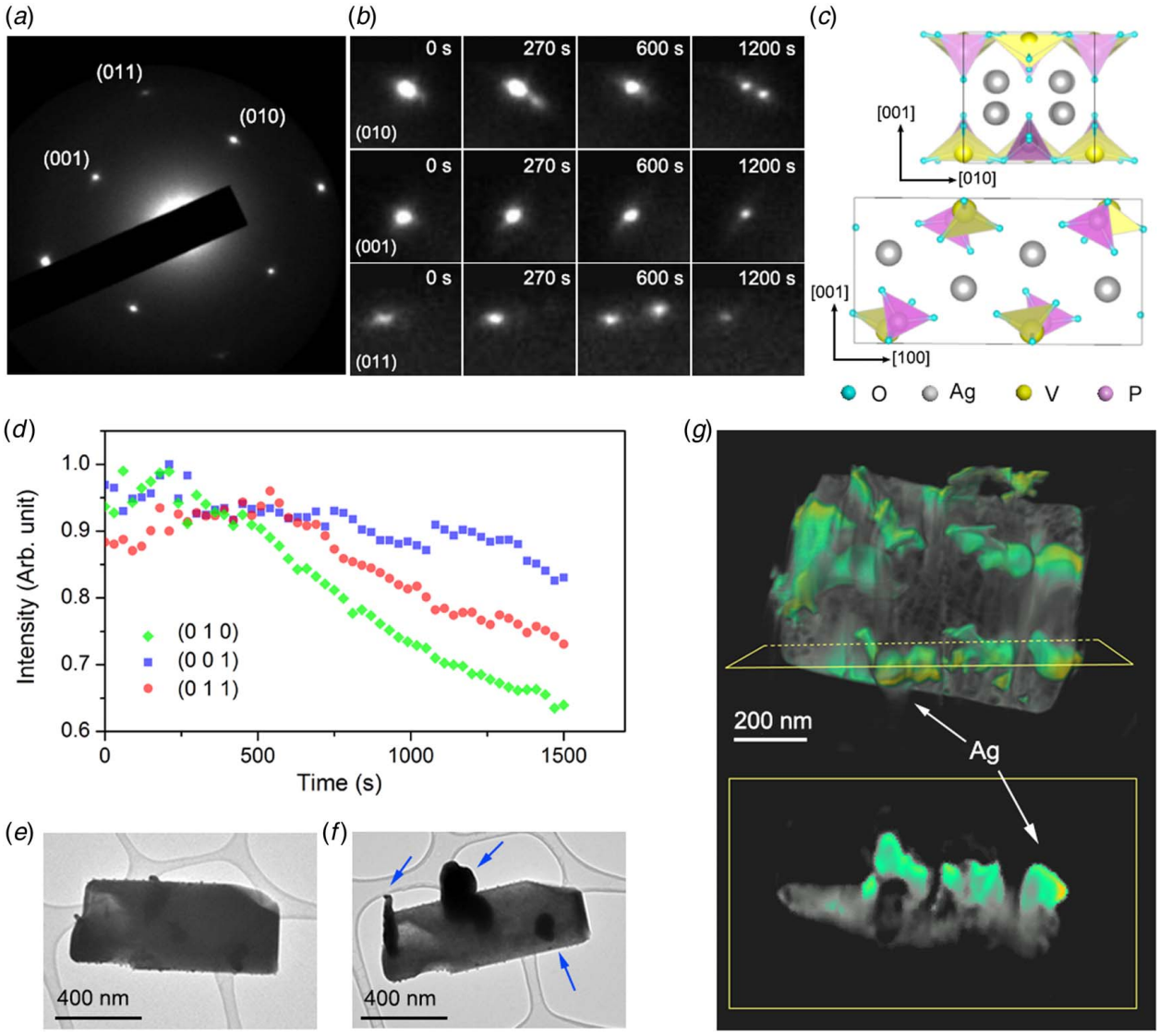

Fig. 5 In situ observation of the Ag reduction and structure evolution under the electron beam. (*a*) Single crystal electron diffraction of $Ag_2VO_2PO_4$ crystal. Zone axis is [1 0 0]. (*b*) Real-time measurement of (0 1 0), (0 0 1), and (0 1 1) diffraction. (*c*) Crystal structure of $Ag_2VO_2PO_4$. (*d*) Integrated diffraction intensity of (0 0 1), (0 1 0), and (0 1 1) diffraction as shown in (*b*), which shows non-exponential decay. (e) and (*f*) TEM images reveal the Ag growth under electron beam irradiation. After 25 min of electron beam illumination, Ag is marked by blue arrows in (*f*). (*g*) Reconstructed three-dimensional crystal after 25 min of electron beam illumination. Green colored part indicates the Ag location. The top panel shows a side view. The bottom panel shows an orthogonal view of a slice of crystal as marked by the yellow outline shown in the top panel image, which shows that the crystal becomes a porous matrix after Ag is reduced and diffused.

was rested at the image center when performing beam alignment; a significant but unknown amount of additional X-ray dose was delivered to this spot in comparison to the other regions during the scanning (0.1 s dwell time for single pixel). This extra illumination resulted in the Ag deficiency. After this initial discovery, we intentionally rested the beam for another 3 min at the exact location. Ag deficiency became more visible (Fig. 3(*c*)). In addition, a few other Ag-rich sites showed up (blue arrows in Fig. 3(*c*)), providing evidence of the Ag aggregation (via diffusion) on the crystal surface (away from the beam center). The observation demonstrated the photo-induced Ag reduction in the material: $Ag^+ + e \rightarrow Ag$.

We also observed V deficiency site in Fig. 3(*c*), presumably arising from the structural collapse or atomic density reduction due to Ag removal. To check the repeatability of the beam effect, we shifted the beam center below the initial position, rested the beam for 10 min, and performed the third fluorescence imaging scan. As shown in Fig. 3(*d*), the XRF images show a similar spot with Ag and V deficiency.

Interestingly, the first beam center, which was deficient in Ag, has now been "filled" with Ag, indicating the existence of mobile Ag on the surface. The Ag map shows a weak stripe-like pattern (slightly lower in Ag concentration), as seen in Fig. 3(*d*). In a separate scan with an enlarged field of view (Fig. 3(*e*)), the weak stripe-like pattern and Ag "filling" were clearly visible. The reason for forming this stripe pattern is unclear and merits further study. It is most likely due to pre-existing defects on the sample surface. On the other hand, we did not observe V "filling" over the beam centers.

We conducted a TXM experiment to determine whether the full-field imaging at the nanoscale can create a similar beam effect [33]. Although the amount of energy transferred to the sample in TXM is similar to the monochromatic diffraction experiment and higher than HXN experiment, we observe no visible morphology change after 40 min of exposure to two crystals as shown in Fig. 4. This can be attributed to the low area radiation density of the X-ray beam in TXM, which is about two and four orders smaller than

the monochromatic diffraction and HXN experiments. Therefore, it is expected that the radiation-induced reaction is drastically slowed down. In addition, TXM has relatively low detection limit (~1%) as a bright field imaging technique, which is primarily sensitive to the material density. In comparison, dark field imaging techniques such as fluorescent imaging at HXN can detect elemental concentration change in the order of one part per million. It is not surprising that TXM measurement did detect a measurable radiation effect on the sample.

Table 1 lists all the X-ray techniques used in our research, including white and monochromatic beam XRD, nano-beam XRF imaging at HXN, and full-field imaging using TXM. The beam size, beam flux, energy density, etc. are included to compare. HXN has the smallest total energy transfer from X-ray to material (1.2×10^{-8} W). However, the energy density is two orders larger than the mono-beam diffraction and four orders larger than TXM. The partial healing effect observed by the HXN (filling of Ag over the beam center) may also be accompanied or, at the least, related by the recovery of diffraction intensity observed in the mono-beam diffraction measurement. In contrast, the white beam Laue diffraction experiment delivered the highest total energy and energy density. Based on the FEA modeling and the measurement data, we conclude that photon-induced Ag reduction and thermal-induced crystal structure degradation are likely to occur simultaneously in the white beam Laue diffraction experiment.

2.3 Structure Evolution Under Electron Beam. We hypothesize that the photon-induced electrons are responsible for reducing Ag ions in $Ag_2VO_2PO_4$ and generating elemental Ag. We thus exposed the sample under electron beams and inspected its structure change using TEM. Figure 5(*a*) shows the electron diffraction pattern of a piece of $Ag_2VO_2PO_4$ single crystal. The zone axis is [1 0 0]. Figure 5(*b*) shows the time series of (0 1 0), (0 0 1), and (0 1 1) diffraction with the electron beam illumination over 0, 270, 600, and 1200 s. Figure 5(*b*) shows the splitting and intensity loss of the (0 1 0) and (0 1 1) diffraction, indicating the formation of crystalline domains with different orientations while also losing the crystalline volume fraction. In contrast, we only observe an intensity decrease for the (0 0 1) diffraction. This difference could arise from the anisotropic structure of the $Ag_2VO_2PO_4$ crystal. As shown in Fig. 5(*c*), in this layered structure, [1 0 0] and [0 1 0] provide the channels for mobile Ag atoms that are reduced. The Ag channeling could be accommodated without significantly perturbing the crystalline lattice in this particular direction. Such an anisotropic lattice structure could explain why we do not observe the peak splitting for the (0 0 1) diffraction. It is also worth noting that the decrease of diffraction intensity does not follow an exponential decay (Fig. 5(*d*)), indicating that no critical dose can characterize the change in structure. It is in sharp contrast to the case of biomaterials and other soft materials [34], in which the diffraction follows the exponential decay due to the destructive electron beam effect. In Fig. 5(*d*), we note that in the first ~500 s, the intensity of the three diffraction peaks did not decrease significantly, possibly because the reaction front (Ag diffusion and reduction at crystal surface) had not reached the region where the diffraction signals were generated and therefore introduced small structure perturbation. After 500 s, all three diffraction spots decrease the intensities monotonously but with different decay rates. The fast decrease in (0 1 0) diffraction indicates significant structure loss in the (0 1 0) plane (refer to Fig. S9 available in the Supplemental Materials on the ASME Digital Collection). This can be attributed to the continued removal of Ag induced by fast Ag diffusion in [1 0 0] direction to form metallic Ag at the crystal surface. In contrast, referring to the atomic structure shown in Fig. S9 in Supporting Information, the structural arrangement in (0 0 1) plane is much more stable against the loss of Ag atoms in the crystalline lattice. This could explain why (0 0 1) diffraction intensity has a slow decay rate.

Figures 5(*e*) and 5(*f*) compare the morphology of a pristine crystal and Ag formation of the sample after 25 min of illumination by the electron beam. We can rule out the direct knock-out effect from the incident electron beam. Under the assumption of binary collision, the maximum energy transferred from electron to atom can be calculated as [35]

$$E = \frac{2(E_e + 2m_e c^2)E_e}{Mc^2}$$

where E_e is the incident electron energy, m_e is the electron mass, c is the speed of light, and M is the mass of the target atom. In our TEM measurements, the energy transferred to an Ag ion is estimated to be 2.7 eV for an electron accelerated at 120 keV and 4.8 eV for an electron accelerated at 200 keV. The transferred energy is well below the energy threshold for an atom to get knocked out through direct momentum transfer, 20–50 eV in typical solids for transition metal ions [36]. Consequently, we confirm that the external electrons induce Ag accumulation. Figure 5(*g*) shows a 3D reconstruction of the crystal after substantial Ag reduction by 25 min of electron beam illumination. The cross-sectional view of the sample on the bottom of Fig. 5(*g*) shows that the reduced Ag atoms form clusters on the (1 0 0) crystal surface, which was oriented perpendicular to the incident electron beam. Since the pristine crystal is highly insulating, the negative potential induced by the secondary electrons accumulated at the surface provides preferential Ag reduction sites. As the Ag atoms are highly mobile in the [1 0 0] direction, a continuous flow of Ag ions can be maintained as the Ag ions at the top surface are reduced by the e-beam. After the Ag removal, the remaining structure is inclined to form a disordered structure due to the structure collapse, as shown in the reconstructed slice plane in the lower panel in Fig. 5(*g*).

3 Conclusions

We have conducted in situ characterizations using X-rays and electrons and explored the effects of the beam on the structural and chemical change. By taking advantage of the state-of-the-art synchrotron radiation sources, structure amorphization and Ag reduction are observed in the sample system of $Ag_2VO_2PO_4$ by submicron diffraction using a white and monochromatic beam. We resolve the nucleation of Ag reduction and redistribution in the sample using a 15 nm X-ray beam. We also distinguish the X-ray-induced thermal effect (at beam density $\sim 10^{-8}$ W nm^{-2}) and the photoelectronic effect (at beam density $\sim 10^{-11}$ W nm^{-2}), further supported by in situ TEM investigation. The work presented here is an example of research into the radiation-induced effects using advanced synchrotron-based X-ray techniques. Continuing enhancement of the synchrotron source brightness presents the opportunities for advancing not only the resolutions for direct imaging but also performing more quantitative investigations on the radiation effects so that the induced material response can be quantitatively distinguished from the reactions produced by the external controls, particularly for the energy materials that are prone to the radiation effects. As a final remark, the beam–material interaction is complex and material specific. Here are some general strategies we can suggest in dealing with potential beam effects. First, one should consider characterization methods that will deliver minimal dose required for extracting the critical information. Try to avoid white beam exposure if alternate mono-beam characterization methods are possible and reduce the beam flux using absorbers whenever appropriate. One should develop criteria for testing the beam effect. It could be the reproducibility of the measurement results with respect to different dose levels or in comparison with the pristine sample or the new locations of the sample without prior beam exposure. Without appropriate validation of the radiation-induced effects, the results from the X-ray or electron characterizations could give misleading interpretations, particularly for in situ experiments, where scientific conclusions are drawn based on the evolution of the sample response to the external controls.

4 Experiments

Sample preparation: $Ag_2VO_2PO_4$ sample powder was sonicated in ethanol, forming a uniform suspension. A drop of the ethanol solution was drop-casted onto a silicon nitride membrane substrate. After completely dried in the air, the sample was used in all X-ray experiments. TEM sample was prepared by drop-casting the ethanol solution on a standard TEM Cu grid and completely dried in air.

White/monochromatic XRD were conducted at beamline 34-ID at Advanced Photon Source (APS) in Argonne National Laboratory. A white X-ray beam in an energy range of 7–40 keV was focused to 500 nm by two K-B mirrors. Beam flux was estimated to be 6×10^{13} photons s^{-1}. A CCD detector was installed in the forward direction to capture the diffraction pattern sample crystal. Energy-adjustable monochromatic X-rays with beam flux of $\sim 1 \times 10^9$ photons s^{-1} were used to scan individual diffraction spots to derive the crystalline lattice deformation. In the experiment, we alternately used the white and monochromatic beams to study the beam-induced effect on the change in material structure. The first Laue diffraction pattern of a pristine $Ag_2VO_2PO_4$ sample was collected using a white beam. The energy transferred to the crystal is estimated as ~3 mJ within 1 s of exposure. Immediately after the first exposure, four successive monochromatic beam scans in the energy range of 13–20 keV were conducted to inspect the (1–10) diffraction spot. Each acquisition lasted about 16 min, which transferred ~0.05 mJ of energy to the crystal. After the monochromatic beam scans, we switched to the white beam and illuminated the sample continuously for 5 min, and then we switched back to the monochromatic beam to check the (1–10) diffraction again. We estimate ~0.9 J of energy transfer under a 5-min white beam illumination. We continued the alternating white/monochromatic beam scans for few times. There were five times white beam exposure throughout the measurement: 1-s exposure for collecting the first Laue diffraction pattern, three 5-min exposures, and 1-s exposure for collecting the final Laue diffraction pattern. In between, we performed nine monochromatic energy scans in total, and each took 16 min. Figure 1(*d*) illustrates the scan sequence.

HXN experiment is performed at beamline 3-ID at NSLS-II in Brookhaven National Laboratory. In the HXN experiment, a monochromatic beam (12 keV) at a flux of $\sim 2 \times 10^8$ photons s^{-1} is focused to 15×15 nm by two orthogonal multilayer Laue lenses. The silicon drift detector is positioned at an angle of 15 deg off the sample plane to collect the X-ray fluorescence signal.

TXM experiment is performed at 32-ID-C beamline at Advanced Photon Source in Argonne National Laboratory. Images were recorded at 8 keV.

TEM experiment is conducted on JEOL-2100F located at the Center for Functional Nanomaterials (CFN) in Brookhaven National Laboratory. The acceleration voltage is either 200 keV or 120 keV.

Acknowledgment

The research used the HXN beamline at 3-ID of the National Synchrotron Light Source II and the CFN resources, which are the U.S. Department of Energy Office of Science User Facilities, at Brookhaven National Laboratory under Contract No. DE-SC0012704. This research is also partially supported by the Laboratory Directed Research and Development (LDRD15-037) program at the Brookhaven National Laboratory. This research used 32-ID-C and 34-ID-C of the APS, a US Department of Energy (DOE) Office of Science User Facility operated for the D.O.E. Office of Science by Argonne National Laboratory under Contract No. DE-AC02-06CH11357. The authors acknowledge the support of the Center for Mesoscale Transport Properties, funded by the U.S. Department of Energy, Office of Science, Basic Energy Sciences, under Award #DE-SC0012673 for the synthesis of the samples. E.S.T. acknowledges support as the William and Jane Knapp Chair in Energy and the Environment.

Conflict of Interest

There are no conflicts of interest.

Data Availability Statement

The datasets generated and supporting the findings of this article are obtainable from the corresponding author upon reasonable request.

References

[1] Courtney, I. A., and Dahn, J. R., 1997, "Electrochemical and In Situ X-Ray Diffraction Studies of the Reaction of Lithium With Tin Oxide Composites," J. Electrochem. Soc., **144**(6), pp. 2045–2052.
[2] Orikasa, Y., Maeda, T., Koyama, Y., Minato, T., Murayama, H., Fukuda, K., Tanida, H., et al., 2013, "Phase Transition Analysis Between $LiFePO_4$ and $FePO_4$ by In-Situ Time-Resolved X-Ray Absorption and X-Ray Diffraction," J. Electrochem. Soc., **160**(5), pp. A3061–A3065.
[3] Chueh, W. C., El Gabaly, F., Sugar, J. D., Bartelt, N. C., McDaniel, A. H., Fenton, K. R., Zavadil, K. R., Tyliszczak, T., Lai, W., and McCarty, K. F., 2013, "Intercalation Pathway in Many-Particle $LiFePO_4$ Electrode Revealed by Nanoscale State-of-Charge Mapping," Nano Lett., **13**(3), pp. 866–872.
[4] Kubobuchi, K., Mogi, M., Ikeno, H., Tanaka, I., Imai, H., and Mizoguchi, T., 2014, "Mn L_2,L_3-Edge X-Ray Absorption Spectroscopic Studies on Charge–Discharge Mechanism of Li_2MnO_3," Appl. Phys. Lett., **104**(5), p. 053906.
[5] Hy, S., Cheng, J. H., Liu, J. Y., Pan, C. J., Rick, J., Lee, J. F., Chen, J. M., and Hwang, B. J., 2014, "Understanding the Role of Ni in Stabilizing the Lithium-Rich High-Capacity Cathode Material $Li[Ni_xLi_{(1-2x)/3}Mn_{(2-x)/3}]O_2$ ($0<=x<=0.5$)," Chem. Mater., **26**(24), pp. 6919–6927.
[6] Lee, E. S., Nam, K. W., Hu, E. Y., and Manthiram, A., 2012, "Influence of Cation Ordering and Lattice Distortion on the Charge–Discharge Behavior of $LiMn_{1.5}Ni_{0.5}O_4$ Spinel Between 5.0 and 2.0 V," Chem. Mater., **24**(18), pp. 3610–3620.
[7] Zhou, Y. N., Ma, J., Hu, E. Y., Yu, X. Q., Gu, L., Nam, K. W., Chen, L. Q., Wang, Z. X., and Yang, X. Q., 2014, "Tuning Charge–Discharge Induced Unit Cell Breathing in Layer-Structured Cathode Materials for Lithium-Ion Batteries," Nat. Commun., **5**(1), p. 5381.
[8] Andersson, A. S., and Thomas, J. O., 2001, "The Source of First-Cycle Capacity Loss in $LiFePO_4$," J. Power Sources, **97–98**, pp. 498–502.
[9] Lin, F., Markus, I. M., Nordlund, D., Weng, T. C., Asta, M. D., Xin, H. L. L., and Doeff, M. M., 2014, "Surface Reconstruction and Chemical Evolution of Stoichiometric Layered Cathode Materials for Lithium-Ion Batteries," Nat. Commun., **5**(1), p. 3529.
[10] Sathiya, M., Abakumov, A. M., Foix, D., Rousse, G., Ramesha, K., Saubanere, M., Doublet, M. L., et al., 2015, "Origin of Voltage Decay in High-Capacity Layered Oxide Electrodes," Nat. Mater., **14**(2), pp. 230–238.
[11] Wang, J. J., Chen-Wiegart, Y. C. K., and Wang, J., 2014, "In Operando Tracking Phase Transformation Evolution of Lithium Iron Phosphate With Hard X-Ray Microscopy," Nat. Commun., **5**(1), p. 4570.
[12] Wang, J. J., Chen-Wiegart, Y. C. K., and Wang, J., 2013, "In Situ Chemical Mapping of a Lithium-Ion Battery Using Full-Field Hard X-Ray Spectroscopic Imaging," Chem. Commun., **49**(58), pp. 6480–6482.
[13] Meirer, F., Cabana, J., Liu, Y. J., Mehta, A., Andrews, J. C., and Pianetta, P., 2011, "Three-Dimensional Imaging of Chemical Phase Transformations at the Nanoscale With Full-Field Transmission X-Ray Microscopy," J. Synchrotron. Radiat., **18**(5), pp. 773–781.
[14] Wang, J. J., Chen-Wiegart, Y. C. K., and Wang, J., 2014, "In Situ Three-Dimensional Synchrotron X-Ray Nanotomography of the (De)Lithiation Processes in Tin Anodes," Angew. Chem. Int. Ed., **53**(17), pp. 4460–4464.
[15] Wang, J. J., Eng, C., Chen-Wiegart, Y. C. K., and Wang, J., 2015, "Probing Three-Dimensional Sodiation-Desodiation Equilibrium in Sodium-Ion Batteries by In Situ Hard X-Ray Nanotomography," Nat. Commun., **6**(1), p. 7496.
[16] Qian, D. N., Ma, C., More, K. L., Meng, Y. S., and Chi, M. F., 2015, "Advanced Analytical Electron Microscopy for Lithium-Ion Batteries," NPG Asia Mater., **7**(6), p. e193.
[17] Mesu, J. G., Beale, A. M., de Groot, F. M. F., and Weckhuysen, B. M., 2006, "Probing the Influence of X-Rays on Aqueous Copper Solutions Using Time-Resolved in Situ Combined Video/X-Ray Absorption Near-Edge/Ultraviolet-Visible Spectroscopy," J. Phys. Chem. B, **110**(35), pp. 17671–17677.
[18] Le Caer, S., 2011, "Water Radiolysis: Influence of Oxide Surfaces on H_2 Production Under Ionizing Radiation," Water, **3**(1), pp. 235–253.
[19] Griscom, D. L., 1985, "Diffusion of Radiolytic Molecular-Hydrogen as a Mechanism for the Post-Irradiation Buildup of Interface States in SiO_2-on-Si Structures," J. Appl. Phys., **58**(7), pp. 2524–2533.
[20] Chen, H. M., Wang, G. D., Chuang, Y. J., Zhen, Z. P., Chen, X. Y., Biddinger, P., Hao, Z. L., et al., 2015, "Nanoscintillator-Mediated X-Ray Inducible Photodynamic Therapy for In Vivo Cancer Treatment," Nano Lett., **15**(4), pp. 2249–2256.
[21] Mcconnell, H. M., Heller, C., Cole, T., and Fessenden, R. W., 1960, "Radiation Damage in Organic Crystals. I. $CH(COOH)_2$ in Malonic Acid," J. Am. Chem. Soc., **82**(4), pp. 766–775.

[22] Berclaz, T., Bernardinelli, G., Celalyanberthier, A., and Geoffroy, M., 1988, "Radiation Damage in Organic Phosphates. Crystal Structure of 3-O-Diphenoxyphosphoryl-1,2-O-Isopropylidene 5-O-Trityl-Alpha-D-Ribofuranose and an Electron Spin Resonance Study of the X-Irradiated Single-Crystal," J. Chem. Soc. Faraday Trans. 1 F, **84**(11), pp. 4105–4113.
[23] Egerton, R. F., Li, P., and Malac, M., 2004, "Radiation Damage in the TEM and SEM," Micron, **35**(6), pp. 399–409.
[24] Kiryukhin, V., Casa, D., Hill, J. P., Keimer, B., Vigliante, A., Tomioka, Y., and Tokura, Y., 1997, "An X-Ray-Induced Insulator-Metal Transition in a Magnetoresistive Manganite," Nature, **386**(6627), pp. 813–815.
[25] Qiao, R. M., Chuang, Y. D., Yan, S. S., and Yang, W. L., 2012, "Soft X-Ray Irradiation Effects of Li_2O_2, Li_2CO_3 and Li_2O Revealed by Absorption Spectroscopy," PLoS One, **7**(11), p. e49182.
[26] Nelson, J., Yang, Y., Misra, S., Andrews, J. C., Cui, Y., and Toney, M. F., 2013, "Identifying and Managing Radiation Damage During In Situ Transmission X-Ray Microscopy of Li-Ion Batteries," Proceedings of SPIE, X-Ray Nanoimaging: Instruments and Methods, San Diego, CA, Vol. 8851, p. 88510B.
[27] Lin, F., Markus, I. M., Doeff, M. M., and Xin, H. L. L., 2014, "Chemical and Structural Stability of Lithium-Ion Battery Electrode Materials Under Electron Beam," Sci. Rep., **4**(1), p. 5694.
[28] Kang, H. Y., Wang, S. L., Tsai, P. P., and Lii, K. H., 1993, "Hydrothermal Synthesis, Crystal-Structure and Ionic-Conductivity of $Ag_2VO_2PO_4$—A New Layered Phosphate of Vanadium(V)," J. Chem. Soc. Dalton Trans., **10**(1), pp. 1525–1528.
[29] Yan, H. F., Bouet, N., Zhou, J., Huang, X. J., Nazaretski, E., Xu, W. H., Cocco, A. P., Chiu, W. K. S., Brinkman, K. S., and Chu, Y. S., 2018, "Multimodal Hard X-Ray Imaging With Resolution Approaching 10 nm for Studies in Material Science," Nano Futures, **2**(1), p. 011001.
[30] Victor, T. W., Easthon, L. M., Ge, M., O'Toole, K. H., Smith, R. J., Huang, X., Yan, H., Allen, K. N., Chu, Y. S., and Miller, L. M., 2018, "X-Ray Fluorescence Nanotomography of Single Bacteria With a Sub-15 nm Beam," Sci. Rep., **8**(1), p. 13415.
[31] Huang, Z. F., Bartels, M., Xu, R., Osterhoff, M., Kalbfleisch, S., Sprung, M., Suzuki, A., et al., 2015, "Grain Rotation and Lattice Deformation During Photoinduced Chemical Reactions Revealed by In Situ X-Ray Nanodiffraction," Nat. Mater., **14**(7), pp. 691–695.
[32] Nazaretski, E., Lauer, K., Yan, H., Bouet, N., Zhou, J., Conley, R., Huang, X., et al., 2015, "Pushing the Limits: An Instrument for Hard X-Ray Imaging Below 20 nm," J. Synchrotron. Radiat., **22**(2), pp. 336–341.
[33] Chu, Y. S., Yi, J. M., De Carlo, F., Shen, Q., Lee, W. K., Wu, H. J., Wang, C. L., et al., 2008, "Hard X-Ray Microscopy With Fresnel Zone Plates Reaches 40 nm Rayleigh Resolution," Appl. Phys. Lett., **92**(10), p. 103119.
[34] Wu, M. H., Liu, N., Xu, G., Ma, J., Tang, L. A., Wang, L. A., and Fu, H. Y., 2011, "Kinetics and Mechanisms Studies on Dimethyl Phthalate Degradation in Aqueous Solutions by Pulse Radiolysis and Electron Beam Radiolysis," Radiat. Phys. Chem., **80**(3), pp. 420–425.
[35] Montet, G. L., and Myers, G. E., 1971, "Threshold Energy for the Displacement of Surface Atoms in Graphite," Carbon, **9**(2), pp. 179–183.
[36] Andersen, H. H., 1979, "The Depth Resolution of Sputter Profile," Appl. Phys., **18**(2), pp. 131–140.